

# Transferring Biomarker into Molecular Probe: Melanin Nanoparticle as a Naturally Active Platform for Multimodality Imaging

Quli Fan,<sup>†,‡,§</sup> Kai Cheng,<sup>†,§</sup> Xiang Hu,<sup>†</sup> Xiaowei Ma,<sup>†</sup> Ruiping Zhang,<sup>†</sup> Min Yang,<sup>†</sup> Xiaomei Lu,<sup>‡</sup> Lei Xing,<sup>§</sup> Wei Huang,<sup>‡</sup> Sanjiv Sam Gambhir,<sup>†</sup> and Zhen Cheng<sup>\*,†</sup>

<sup>†</sup>Molecular Imaging Program at Stanford (MIPS), Canary Center at Stanford for Cancer Early Detection, Department of Radiology and Bio-X Program, School of Medicine, Stanford University, Stanford, California 94305-5484, United States

<sup>‡</sup>Key Laboratory for Organic Electronics & Information Displays and Institute of Advanced Materials, Nanjing University of Posts & Telecommunications, Nanjing 210046, China

<sup>§</sup>Department of Radiation Oncology, School of Medicine, Stanford University, Stanford, California 94305, United States

## S Supporting Information



**ABSTRACT:** Developing multifunctional and easily prepared nanoplatforms with integrated different modalities is highly challenging for molecular imaging. Here, we report the successful transfer of an important molecular target, melanin, into a novel multimodality nanoplatform. Melanin is abundantly expressed in melanotic melanomas and thus has been actively studied as a target for melanoma imaging. In our work, the multifunctional biopolymer nanoplatform based on ultrasmall (<10 nm) water-soluble melanin nanoparticle (MNP) was developed and showed unique photoacoustic property and natural binding ability with metal ions (for example, <sup>64</sup>Cu<sup>2+</sup>, Fe<sup>3+</sup>). Therefore, MNP can serve not only as a photoacoustic contrast agent, but also as a nanoplatform for positron emission tomography (PET) and magnetic resonance imaging (MRI). Traditional passive nanoplatforms require complicated and time-consuming processes for prebuilding reporting moieties or chemical modifications using active groups to integrate different contrast properties into one entity. In comparison, utilizing functional biomarker melanin can greatly simplify the building process. We further conjugated α<sub>v</sub>β<sub>3</sub> integrins, cyclic c(RGDfC) peptide, to MNPs to allow for U87MG tumor accumulation due to its targeting property combined with the enhanced permeability and retention (EPR) effect. The multimodal properties of MNPs demonstrate the high potential of endogenous materials with multifunctions as nanoplatforms for molecular theranostics and clinical translation.

## INTRODUCTION

Naturally produced biopolymers in living organisms play crucial roles in materials discovery and development. They have inspired scientists to synthesize novel biomaterials through mimicking Mother Nature, or they can further serve as templates and building blocks to prepare new generations of biocompatible, bioregenerative, or biodegradable materials for biomedical applications. For instance, DNA has been used to rationally design plasmonic nanostructures,<sup>1</sup> to build nanoscaffolds for incorporating multiple-affinity ligands,<sup>2</sup> and to self-assemble into numerous prescribed 3D shapes.<sup>3</sup> Cellular membranes have also been widely imitated by phospholipids and polysaccharides to form liposome or micelles for drug and imaging agent delivery.<sup>4,5</sup> Leukocyte membranes have also been

used to coat silicon nanoparticles (NPs) to yield hybrid NPs that achieve cell-like functions, including avoiding clearance by the immune system.<sup>6</sup> All these studies highlight the power of biomimicry for development of novel biomaterials.

Multimodal imaging combines different modalities together to provide complementary information and achieve synergistic advantages over any single modality alone. It has emerged as a very promising strategy for preclinical research and clinical applications.<sup>7</sup> One major challenge of multimodal imaging is to develop an efficient platform to load various components with individual contrast properties together while maintaining

Received: May 29, 2014

Published: October 7, 2014



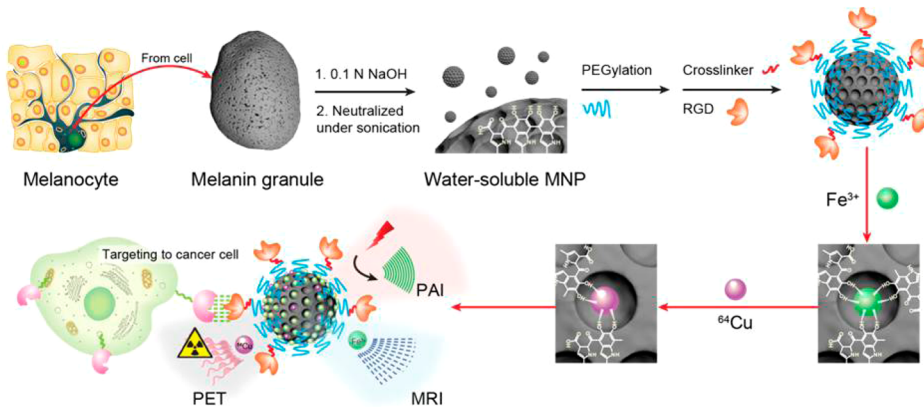


**Figure 1.** Multimodality molecular imaging of MNPs. The melanin granules were first dissolved in 0.1 N NaOH aqueous solution, and then neutralized under sonication to obtain melanin nanoparticles in high water monodispersity and homogeneity. After PEG surface-modification, RGD was further attached to the MNP for tumor targeting. Then  $\text{Fe}^{3+}$  and/or  ${}^{64}\text{Cu}^{2+}$  were chelated to the obtained MNPs for PAI/MRI/PET multimodal imaging.

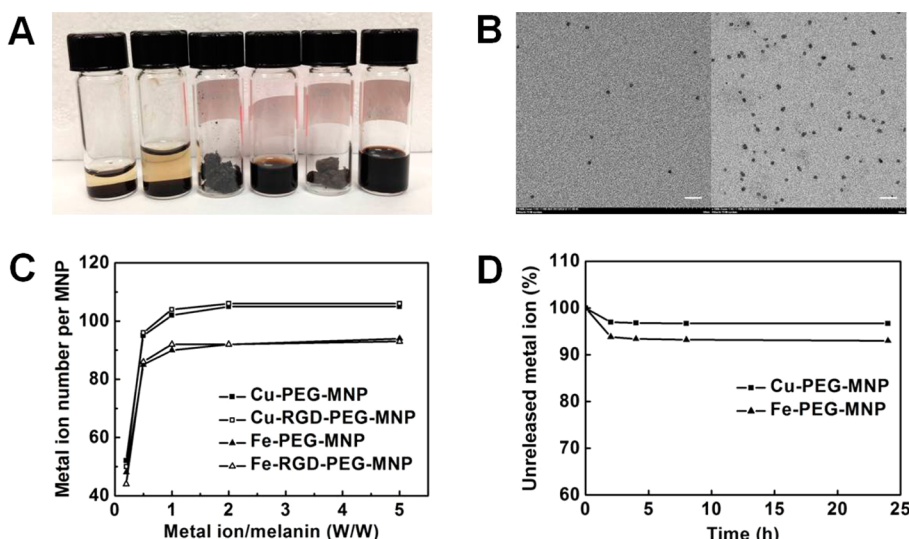


**Figure 2.** Characterization of physical properties of MNPs. (A) From left to right: pictures of (1) pristine melanin granule in  $\text{H}_2\text{O}$ , (2) melanin neutralized without sonication in  $\text{H}_2\text{O}$ , (3) freeze-dried PWS-MNP, (4) freeze-dried PWS-MNP redissolved in PBS ( $\text{pH} = 7.4$ ), (5) freeze-dried PEG-MNP, (6) freeze-dried PEG-MNP redissolved in PBS ( $\text{pH} = 7.4$ ). (B) TEM of PWS-MNP (left) and PEG-MNP (right), scale bar = 20 nm. (C) The plot of the relationship between the number of metal ions attached on one MNP with feed ratio ( $W_{\text{ions}}: W_{\text{MNP}}$ ). (D) Stability study of metal ion-chelated MNPs in PBS ( $\text{pH} = 7.4$ ).

compact size, good biocompatibility and targeting capability. A variety of nanomaterials have been explored for multimodal imaging. In particular, exogenous inorganic NPs-based reporters have attracted considerable interests,<sup>8–11</sup> such as iron oxide NPs for magnetic resonance imaging (MRI) and quantum dots for fluorescence imaging. Compared with inorganic NPs, organic NPs generally exhibit good biocompatibilities, biodistribution and clearance, although most of them only appear to possess optical imaging properties.<sup>12</sup> Some biomolecules based NPs such as liposomes have been widely used for loading contrast agents and drugs. But they themselves lack intrinsic contrast properties and only function as carriers. Therefore, such biomolecules need complicated and time-consuming processes to prebuild various contrast properties or require chemical modifications to integrate different reporting moieties into one entity, which we term as a passive platform. For example, organic ligands are generally incorporated into a nanoparticle before chelating to radioactive or magnetic metal

ions for positron emission tomography (PET)<sup>13</sup> and magnetic resonance imaging (MRI).<sup>14</sup>

Melanin, an amorphous, irregular functional biopolymer and a ubiquitous natural pigment that presents in many organisms including human skin, is a typical biomarker for disease imaging including melanoma detection and Parkinson diseases diagnosis.<sup>15–17</sup> In this study, we report the successful transferring of this biomarker into an imaging nanoplateform.

By mimicking natural melanin, water-soluble melanin nanoparticle (MNP) has been synthesized and used as the active platform for multimodal imaging of tumors. We demonstrate that MNP can not only offer its native optical properties for photoacoustic imaging (PAI), but also actively chelate to metal ions ( ${}^{64}\text{Cu}^{2+}$ ,  $\text{Fe}^{3+}$ ) for PET and MRI with a high loading capacity and stability utilizing its intrinsic chelating function. Furthermore, ultrasmall size MNPs ( $\sim 4.5 \text{ nm}$ ) can be easily prepared and surface-modified. Overall, these unique properties significantly simplify the process of preparation of

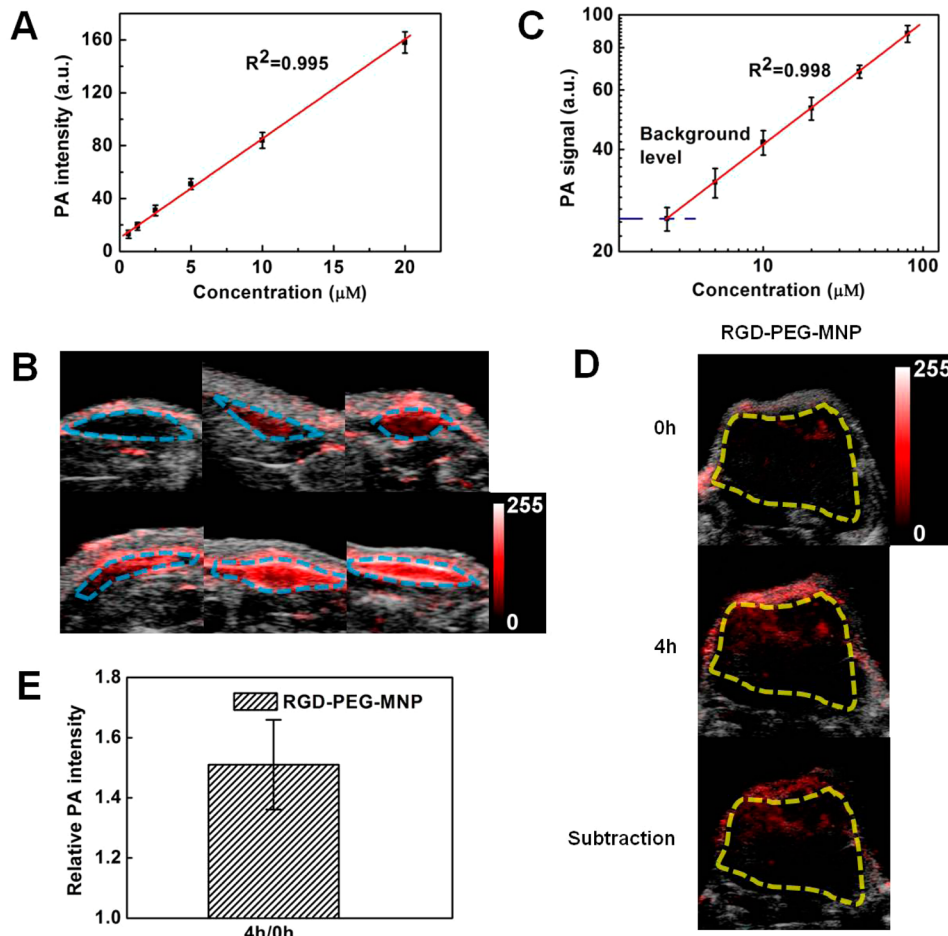


**Figure 3.** In vitro and in vivo study of PAI of MNPs. (A) The photoacoustic signal produced by PEG-MNPs at concentrations of 0.625, 1.25, 2.5, 5.0, 10, and 20  $\mu\text{M}$ , and it was observed to be linearly dependent on its concentration ( $R^2 = 0.995$ ). (B) Photoacoustic detection of PEG-MNP in living mice. Mice were injected subcutaneously (region enveloped by blue dotted line) with PEG-MNP at concentrations of 0, 5, 10 (from left to right in top row), and 20, 40, 80 (from left to right in bottom row)  $\mu\text{M}$ . One vertical slice in the photoacoustic image (red) was overlaid on the corresponding slice in the ultrasound image (gray). (C) The photoacoustic signal from each inclusion was calculated. The background level represents the endogenous signal measured from tissues. The linear regression is calculated on the five most concentrated inclusions ( $R^2 = 0.998$ ). (D) The overlaying of ultrasonic (gray) and photoacoustic (red) imagings of U87MG tumor (region enveloped by yellow dotted line) before and after tail-vein injection of 250  $\mu\text{L}$  of 200  $\mu\text{M}$  RGD-PEG-MNP in living mice ( $n = 3$ ) and their subtraction imagings. (E) Quantitative analysis of enhanced PA signal of U87MG tumor after tail-vein injection with RGD-PEG-MNP at 4 h, compared with at 0 h.

multimodal imaging probes and make MNP a highly promising nanomaterial for biomedical applications.

## RESULTS

**Synthesis and Characterization of MNPs.** Figure 1 schematically illustrates the procedure to prepare ultrasmall water-soluble MNP with multimodal imaging properties. To change the intrinsic poor water-solubility of melanin, pristine melanin granule was first dissolved in a 0.1 N NaOH<sup>18</sup> and then neutralized under the assistance of sonication to decrease interchain aggregation. Ultrasmall MNP in high water monodispersity and homogeneity with a size of  $4.5 \pm 0.5$  nm, which was termed as plain water-soluble MNP (PWS-MNP), were successfully obtained (Figure 2A,B and Figure S1A, Supporting Information). PWS-MNP exhibited excellent water-solubility of 40 mg/mL and stability, which can be attributed to the highly negative potential of approximately  $-22.2$  mV on the NP surface that efficiently blocks the NP aggregation through electrostatic repulsion (Figure S1B). Furthermore, PWS-MNP can be stored as lyophilized powder for over six months and effectively redissolved in water allowing

long-term usage (Figure 2A). The FT-IR spectra of pristine melanin granule and PWS-MNP were similar to each other, indicating no significant change of molecular structure (Figure S2A). The <sup>1</sup>H NMR spectrum of PWS-MNP in D<sub>2</sub>O showed no obvious signal belonging to the hydrogen atom on the arylene groups, suggesting most of the conjugated backbones were buried in the NP (Figure S2B).<sup>19</sup> The molecular weight of a PWS-MNP was calculated from the nanoparticle size and its density (1.3 g/cm<sup>3</sup>), which is about 40 kDa.

To retain the water-solubility of PWS-MNPs for further biomodification and metal ion-chelating, polyethylene glycol (PEG) chains<sup>20</sup> were introduced to the MNP. NH<sub>2</sub>-PEG<sub>5000</sub>-NH<sub>2</sub> was used because the amine groups can react with dihydroxyindole/indolequinone groups in melanin.<sup>21</sup> The number of PEG chains per MNP was determined to be 19 (Figure S3A and S3B). The diameter of the PEG-functionalized MNP (PEG-MNP) became large and reached 7.0 nm (Figure 2B and Figure S1A). Moreover, the surface potential of PEG-MNP decreased to  $-6.1$  mV (Figure S1B) because of introduction of PEG and positive NH<sub>2</sub> groups on the MNP surface. The similar absorption spectrum of PEG-MNP to

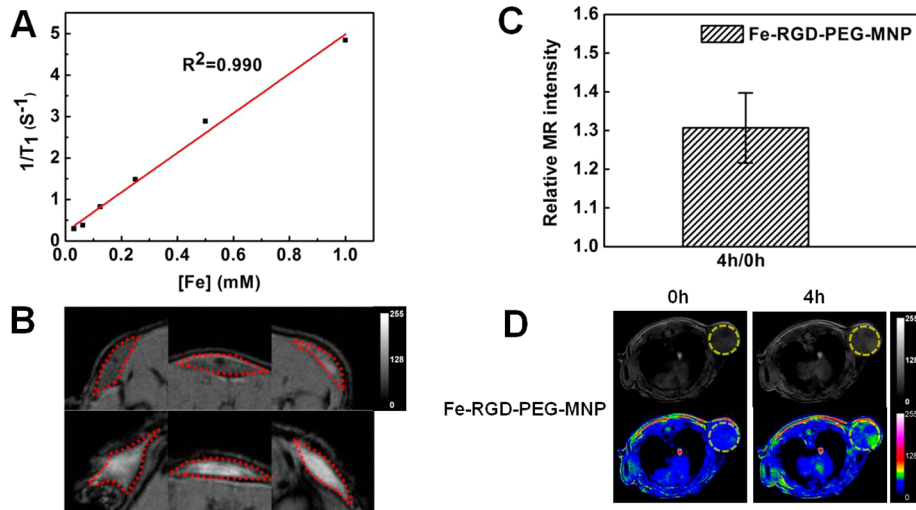


**Figure 4.** In vitro and in vivo study of MRI of  $\text{Fe}^{3+}$ -chelated MNPs. (A)  $T_1$  relaxation rates ( $1/T_1, \text{s}^{-1}$ ) as a function of Fe-RGD-PEG-MNP (mM) in agarose gel (1.0 T, 25 °C). (B) MRI detection of Fe-RGD-PEG-MNPs in living mice. Mice were injected subcutaneously (region enveloped by red dotted line) with Fe-RGD-PEG-MNPs at concentrations of 0, 1.25, 2.5 (from left to right in upper layer), and 5, 10, 20 (from left to right in bottom layer)  $\mu\text{M}$ . (C) Quantitative analysis of enhanced MR signal of U87MG tumor after tail-vein injection with RGD-PEG-MNP at 4 h, compared with 0 h. (D) MRI images of U87MG tumors (region enveloped by yellow dotted line) before and after tail-vein injection of 250  $\mu\text{L}$  of 200  $\mu\text{M}$  RGD-PEG-MNP in living mice ( $n = 3$ ) (TR: 700 ms, TE: 5.2 ms). Top row shows black and white images, and bottom row shows the pseudocolored images.

PWS-MNP demonstrated that the PEG-modification did not influence the absorption properties of melanin (Figure S3C). Lastly, for demonstrating that MNP can be used as a platform for biomodification, PEG-MNP was further modified with biomolecules such as cyclic Arg-Gly-Asp-D-phe-Cys [c-(RGDfC)] peptide (abbreviated as RGD), which can target tumor  $\alpha_v\beta_3$  integrin.<sup>22</sup> The number of RGD attached to the MNP was calculated to be about 8 per MNP and the size of RGD-functionalized PEG-MNP (RGD-PEG-MNP) increased a little to  $\sim 9.6$  nm (Figure S4).

**Chelating to  $\text{Cu}^{2+}$  and  $\text{Fe}^{3+}$ .** To investigate the possibility of MNP as a platform for PET and MRI, its chelating properties to  $\text{Cu}^{2+}$  ( $^{64}\text{Cu}^{2+}$  for PET) and  $\text{Fe}^{3+}$  (for MRI) were studied. After adding metal ions (0.2 mL of 10 mM  $\text{FeCl}_3$  or  $\text{CuCl}_2$ ) into MNP aqueous solutions (1 mL of 20  $\mu\text{M}$  for PWS-MNP and PEG-MNP), the precipitation of PWS-MNP quickly appeared, while PEG-MNP maintained good water-solubility (Figure S5). The  $\text{Fe}^{3+}$  or  $\text{Cu}^{2+}$ -chelated MNP (Fe-PEG-MNP, Fe-RGD-PEG-MNP, Cu-PEG-MNP and Cu-RGD-PEG-MNP) exhibited high loading capacities. The maximum quantities of one MNP to chelate to  $\text{Cu}^{2+}$  and  $\text{Fe}^{3+}$  are about 100 and 90 ions, respectively, no matter whether RGD is attached to the MNP or not (Figure 2C). After  $\text{Fe}^{3+}$ -chelating, the MNP sizes increased to  $\sim 8.9$  nm and  $\sim 10.7$  nm for Fe-PEG-MNP and Fe-RGD-PEG-MNP respectively and their zeta-potential remained in the neutral region (Figure S4 and Table S1).

**Stability and Biocompatibility of MNPs.** The optical stabilities of PEG-MNP and RGD-PEG-MNP under increasing durations of light exposure were further tested. Compared with those reported dyes for PAI, which exhibit significant reduced absorption (>30%) under light exposure,<sup>23</sup> PEG-MNP and RGD-PEG-MNP showed intriguing photostability (only 3% reduced absorption) (Figure S6), indicating their high capability for PAI. Further stability assay of  $\text{Fe}^{3+}$  or  $\text{Cu}^{2+}$ -chelated MNPs in PBS solution showed that only about 3%  $\text{Cu}^{2+}$  and 7%  $\text{Fe}^{3+}$  were released from those MNPs at the first 2 h, and there was no further release at longer incubation time

points, indicating the high stability of the chelating platform (Figure 2D). The first 2 h released metal ions may derive from those that were absorbed on the MNPs through weak electrostatic interaction. Furthermore, the high viability of NIH3T3 and U87MG cells (about 90–110% as compared to the nontoxic control) after 24 h of incubation with PEG-functionalized MNPs was found, indicating high biocompatibility and low cytotoxic effect of PEG-functionalized MNPs (Figure S7).

**PAI of MNPs.** To investigate the possibility of MNPs to be used as a photoacoustic agent, we first studied the detection sensitivity of PEG-MNP in aqueous solution at increasing concentrations from 0.625 to 20  $\mu\text{M}$ . The PEG-MNP with 0.625  $\mu\text{M}$  was detected, and the photoacoustic signals increased linearly with the increase of PEG-MNP concentrations ( $R^2 = 0.995$ ) (Figure 3A).

The detection sensitivity of MNP in living body was further tested by subcutaneous injection of PEG-MNP on the lower back of mice ( $n = 3$ ) at increasing concentrations of 5 to 80  $\mu\text{M}$  (Figure 3B). A linear correlation ( $R^2 = 0.998$ ) between the MNP concentration and the corresponding photoacoustic signal was observed in Figure 3C. The background signal from tissue was quantified using the signals from the areas without injection any contrast agent. 2.5  $\mu\text{M}$  of PEG-MNP was found to give the equivalent photoacoustic signal strength as the tissue background.

To further investigate the in vivo PAI properties, one group of U87MG tumor mice were tail-vein injected with 250  $\mu\text{L}$  of RGD-PEG-MNP at a concentration of 200  $\mu\text{M}$ . Mice showed obvious increase of photoacoustic signal in tumors after injection with RGD-PEG-MNP at 4 h than that of prescan (Figure 3D). The increased photoacoustic signal of RGD-PEG-MNP (Figure 3E) could be attributed to the enhanced permeability and retention (EPR) effect and the tumor targeting ability of RGD-PEG-MNP to  $\alpha_v\beta_3$  integrin. Furthermore, instead of Vevo LAZR PAI System, using Inveon research workplace (NEXUS 128) was able to obtain 3D PA

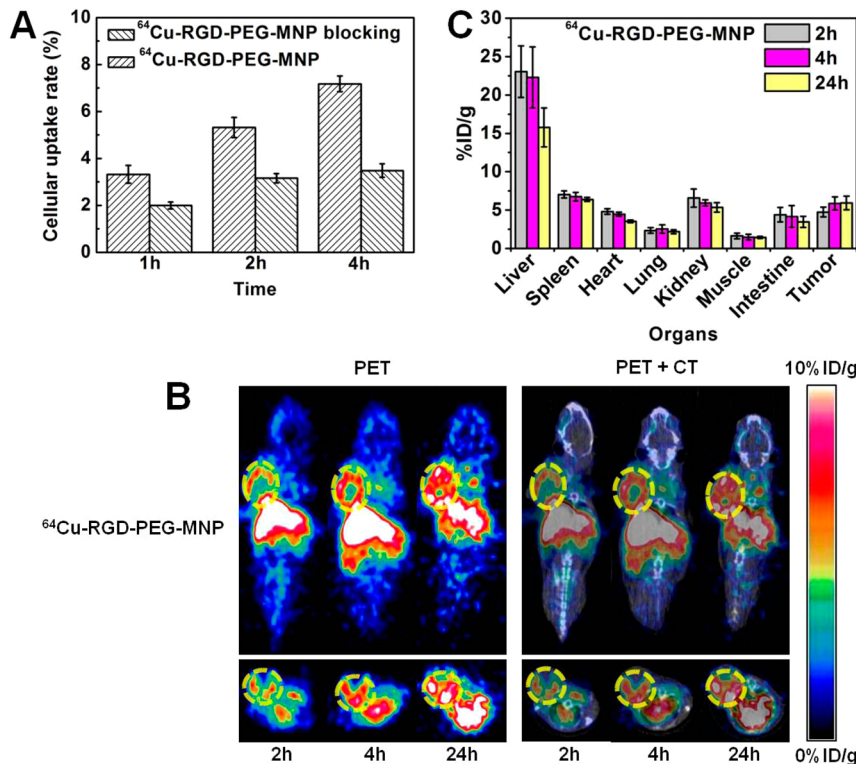


**Figure 5.** In vitro and in vivo study of PET of  $^{64}\text{Cu}$ -labeled MNPs. (A) Uptake of  $^{64}\text{Cu}$ -RGD-PEG-MNP with and without blocking in U87MG cells at 37 °C for 1, 2 and 4 h incubation. All results, expressed as percentage of cellular uptake, are mean of triplicate measurements  $\pm$  SD. (B) Representative decay-corrected coronal (top) and transaxial (bottom) small animal PET images (left three images) and the overlaying of CT (gray) and PET (color) images (right three images) of U87MG tumors (region enveloped by yellow dotted line) acquired at 2, 4, and 24 h after tail vein injection of  $^{64}\text{Cu}$ -RGD-PEG-MNP. (C) Biodistribution of  $^{64}\text{Cu}$ -RGD-PEG-MNP in mice ( $n = 3$ ) at 2, 4, and 24 h after injection. The radioactive signal from each organ was calculated using a region of interest drawn over the whole organ region.

imaging, which provided the more clearly enhanced blood vessel signals in tumor after MNP injection (Figure S8).

**MRI of MNPs.** To study whether  $\text{Fe}^{3+}$  ( $T_1$  contrast agent) retains MR signal-enhancing property after loading into MNPs,  $T_1$ -weighted MRI images of various concentrations of Fe-RGD-PEG-MNP in agarose gel was investigated (Figure S9A). With the increase of NP concentration, MR signal was significantly enhanced, suggesting Fe-RGD-PEG-MNP generate a high magnetic field gradient on their surface.  $R_1$  value of Fe-RGD-PEG-MNP (the slope of the fitted curve in Figure 4A, using  $\text{Gd}^{3+}$  as standard) was calculated to be  $1.2 \text{ mM}^{-1} \text{ s}^{-1}$ .

The magnetic sensitivity in living mice was then tested by subcutaneous injection of Fe-RGD-PEG-MNP on the lower back of mice ( $n = 3$ ) at increasing concentrations of 1.25 to 20  $\mu\text{M}$ . It was extrapolated that 1.25  $\mu\text{M}$  of Fe-RGD-PEG-MNP produced the equivalent MRI signal intensity as the tissue background (Figure 4B).

To demonstrate the use of MNP as the platform for MRI of tumors,  $T_1$ -weighted images were obtained from mice bearing U87MG tumors ( $n = 3$ ). U87MG tumors displayed increased signals after 4 h MNP injection (Figure 4D). The relative MR signal intensity of tumor at 4 h increased 30% compared with at 0 h, demonstrating that MNP can be used as a platform for MRI (Figure 4C). Furthermore, further optimizing the MR imaging conditions can provide more clearly enhanced MRI signal and MNP accumulation in tumor (Figure S9B).

**PET of MNPs.** To investigate the PET imaging properties of MNP,  $^{64}\text{Cu}^{2+}$  was selected as a PET radiolabel for MNP because it can be readily chelated by melanin and the intermediate half-life of  $^{64}\text{Cu}^{2+}$  (12.7 h) makes it suitable for

radiolabeling of biomolecules and imaging.<sup>24–26</sup> Simple mixing of RGD-PEG-MNP and PEG-MNP with  $^{64}\text{Cu}^{2+}$  allowed successfully labeling the NPs in the yield of 80%. The resulting MNPs,  $^{64}\text{Cu}$ -RGD-PEG-MNP and  $^{64}\text{Cu}$ -PEG-MNP, displayed excellent stability in PBS solution (Figure S10). Similar to  $\text{Cu}^{2+}$ -chelated MNPs, only ~3%  $^{64}\text{Cu}^{2+}$  released from the MNPs after 24 h of incubation. Thus,  $^{64}\text{Cu}$ -labeled MNPs were easily and reliably produced and exhibited reasonable stability in vitro.

Uptake of  $^{64}\text{Cu}$ -RGD-PEG-MNP by U87MG cells with or without blocking agent RGD at 1, 2, and 4 h are shown in Figure 5A.  $^{64}\text{Cu}$ -RGD-PEG-MNP exhibited higher uptakes than blocking group at all the incubation time, with a value of  $3.32 \pm 0.37\%$ ,  $5.32 \pm 0.43\%$  and  $7.18 \pm 0.33\%$  for  $^{64}\text{Cu}$ -RGD-PEG-MNP at 1, 2, and 4 h. In comparison, for  $^{64}\text{Cu}$ -RGD-PEG-MNP blocking group, much lower uptake of  $^{64}\text{Cu}$ -RGD-PEG-MNP was observed with a value of  $2.00 \pm 0.15\%$ ,  $3.16 \pm 0.20\%$  and  $3.48 \pm 0.29\%$  at 1, 2, and 4 h, respectively, indicating the successful biomodification of MNPs with RGD peptide and the specific targeting ability of RGD contribute to the uptake of  $^{64}\text{Cu}$ -RGD-PEG-MNP by U87MG cells.

The in vivo PET of MNPs was performed in U87MG-tumor-bearing mice.  $^{64}\text{Cu}$ -RGD-PEG-MNP showed tumor accumulation and clear tumor contrast after 2 h postinjection (Figure 5B). Quantification analysis revealed that the tumor uptake values of  $^{64}\text{Cu}$ -RGD-PEG-MNP gradually increased with time to 24 h, and they were  $4.75 \pm 0.63$ ,  $5.87 \pm 0.87$ , and  $5.93 \pm 0.89\% \text{ ID/g}$  at 2, 4, and 24 h, respectively (Figure 5C). In addition to the tumor, moderate activity accumulation was

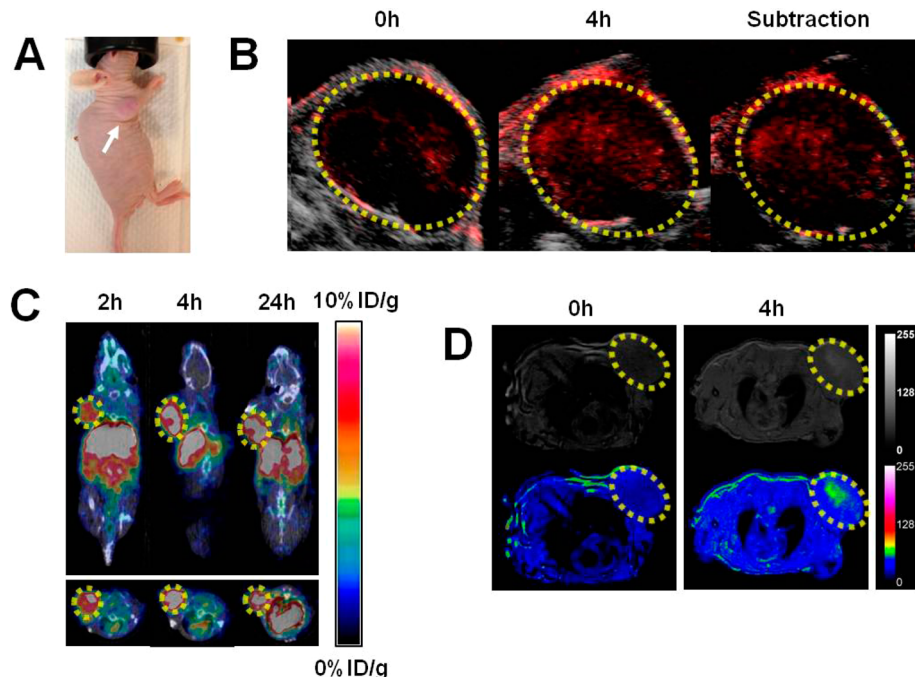


**Figure 6.** In vivo multimodality imaging of tumor (region enveloped by yellow dotted line) bearing mice with PAI and MRI/PET respectively. (A) Photographic images of U87MG tumor bearing mice. (B) The overlaying of ultrasonic (gray) and photoacoustic (red) imaging of U87MG tumor before and after tail-vein injection of  $^{64}\text{Cu}$ -Fe-RGD-PEG-MNP ( $200\ \mu\text{L}$  of  $10\ \mu\text{M}$ ) in living mice and their subtraction imaging. (C) The overlaying of representative decay-corrected coronal (top) and transaxial (bottom) small animal CT (gray) and PET (color) images of U87MG tumors acquired at 2, 4, and 24 h after tail vein injection of  $^{64}\text{Cu}$ -Fe-RGD-PEG-MNP and Fe-RGD-PEG-MNP ( $250\ \mu\text{L}$  of  $200\ \mu\text{M}$ ). (D) MRI images of U87MG tumor before and after tail-vein injection of  $^{64}\text{Cu}$ -Fe-RGD-PEG-MNP and Fe-RGD-PEG-MNP ( $250\ \mu\text{L}$  of  $200\ \mu\text{M}$ ) in living mouse. Top row shows black and white images, and bottom row shows the pseudocolored images. White arrow refers to the tumor position.

observed in the liver (e.g.,  $15.78 \pm 2.55\% \text{ ID/g}$  at 24 h for all MNPs), and relative lower activity accumulation was also found in the kidneys (e.g.,  $5.34 \pm 0.62\% \text{ ID/g}$  at 24 h for all MNPs). These data indicated the MNP was cleared mainly through hepatobiliary system. To further investigate the possible targeting property of MNPs, the  $^{64}\text{Cu}$  radiolabeled RGD-PEG-MNP and control cyclic Arg-Ala-Asp-D-phe-Cys [c-(RADfC)] peptide (abbreviated as RAD, with nontargeting property for tumor  $\alpha,\beta_3$  integrin) functionalized PEG-MNP ( $^{64}\text{Cu}$ -RAD-PEG-MNP) for U87MG tumor PET imaging were compared with each other (Figure S11). The obvious stronger PET signal of  $^{64}\text{Cu}$ -RGD-PEG-MNP can be found in tumor at 4 h than that of  $^{64}\text{Cu}$ -RAD-PEG-MNP ( $P < 0.05$ ), indicating the good and specific targeting property of RGD-PEG-MNP.

**PET and PAI/MRI of  $^{64}\text{Cu}$ -Fe-RGD-PEG-MNP.** To investigate the possibility of using MNP platform for multimodality imaging, MNP were mixed with  $\text{Fe}^{3+}$  and  $^{64}\text{Cu}^{2+}$  in sequence to form the multifunctional probes Fe-RGD-PEG-MNP and  $^{64}\text{Cu}$ -Fe-RGD-PEG-MNP (the amount of  $\text{Fe}^{3+}$  per MNP is 56) for PET/PAI/MRI. PET of mice bearing U87MG tumors were then obtained first at 2, 4, and 24 h postinjection of  $^{64}\text{Cu}$ -Fe-RGD-PEG-MNP. After 48 h,  $T_1$ -weighted MRI and PAI of mice bearing U87MG tumors were then obtained respectively at 4 h after another injection of large dose of Fe-RGD-PEG-MNP. In Figure 6,  $^{64}\text{Cu}$ -Fe-RGD-PEG-MNP showed very similar PET, MRI and PAI properties on U87MG tumor, compared with the corresponding single modality imaging from  $^{64}\text{Cu}$ -RGD-PEG-MNP, Fe-RGD-PEG-MNP, and RGD-PEG-MNP respectively. These results showed that using MNP as the active platform to load  $^{64}\text{Cu}^{2+}$  and  $\text{Fe}^{3+}$  together can efficiently combine its native photoacoustic

properties with radioactive and magnetic properties together for multimodality imaging.

## DISCUSSION

To change the lack of contrast properties of biomolecule-based nanoparticle for multimodality imaging, recently porphyrin were successfully introduced into phospholipid to provide the platform with desirable optical properties,<sup>27–29</sup> while it still requires complicated and time-consuming chemical modifications and other reporting molecules to achieve multimodality imaging ability. We herein developed the functional biomarker, melanin, as a novel nanoparticle with its native optical property and multifunctions, which can simply and actively collecting optical, magnetic and radioactive properties together for multimodality imaging. Melanin, the oxidation products of tyrosine, plays an important role in living organism.<sup>30</sup> Accompanied with the development of molecular imaging probes in the past decade, melanin has been used as an effective molecular target<sup>31–33</sup> as well as endogenous contrast agent for PAI because of its strong light absorption properties.<sup>34,35</sup> Besides, melanin has intrinsic strong chelating properties to many metal ions including  $\text{Cu}^{2+}$  and  $\text{Fe}^{3+}$ <sup>36–38</sup> which can be used to nuclear imaging and MRI. Consequently melanotic melanomas show hyperintensity on  $T_1$ -weighted MRI images.<sup>39,40</sup>

Considering the attractive properties of the biomarker melanin, we and others have engineered cancer cells to biologically produce melanin for multimodality imaging (PAI/MRI/PET) of cancer.<sup>41–43</sup> However, this method requires genetic modification of cells, which is time-consuming and may have limited clinical value. Thus, water-soluble MNPs are more

appropriate to behave as a natural “active platform” to simplify the preparation procedure for multimodal applications. Considering only trace amount of  $^{64}\text{Cu}^{2+}$  ions utilized for PET and its final decay to  $\text{Zn}^{2+}$  ions, which is necessary for life process, and the abundant amount of  $\text{Fe}^{3+}$  ions in living body,  $^{64}\text{Cu}^{2+}$  and  $\text{Fe}^{3+}$  ions used in our system are expected to be metabolized in living subjects. In comparison, although  $\text{Gd}^{3+}$  ion has higher  $T_1$  MRI effect than  $\text{Fe}^{3+}$  ion, its potential toxicity is still a problem. Concomitantly, the traditional nanoparticle-based platform needs complicated functionalization of ligand to chelate  $\text{Gd}^{3+}$  for MRI and  $^{64}\text{Cu}^{2+}$  for PET. More interestingly, the new MNP system can serve as an active nanoplatform and easily bind with metal ions without the traditional needs of surface modification and introducing chelating groups, which significantly simplifies the preparation process and reduces the heterogeneity of the resulting multimodal NPs. Furthermore, the MNP is an organic and biodegradable material and showed relatively good tumor imaging properties. All of these properties make MNPs highly promising for potential clinical translation.

Despite its important functions, developing melanin for molecular imaging was highly subjected to its intrinsic poor water-solubility. Therefore, preparing MNPs is desired while still a challenge for well-dispersing in water, especially for those with size around 10 nm that can provide not only appropriate blood circulation time, but also high surface-to-volume ratio to chelate enough metal ions for efficient bioimaging. Although the formation mechanism of polymeric melanin is not clear, its molecular structure is generally considered to be composed of dihydroxyindole/indolequinone segments with hydrophobic conjugated main chain having strong  $\pi-\pi$  interaction and hydrophilic hydroxyl groups on the benzene rings.<sup>44</sup> Therefore, to realize melanin water-soluble at neutral environments, decreasing the interchain  $\pi-\pi$  aggregation of conjugated main chains and lowering the formed melanin particle size to expose more hydrophilic hydroxy groups on the surface of melanin is a promising way. In our work, we first realized the synthesis of ultrasmall MNPs in water with high monodispersity and homogeneity under the assistance of sonication. Another problem that should be resolved is the metal ion-initiated cross-linking and the formation of MNP precipitation. Recent reports showed that  $\text{Fe}^{3+}$  is a strong cross-linker for catechol groups,<sup>45</sup> which is one of the components in melanin molecular structure. In our work, PEG encapsulation is found can not only enhance the biocompatibility and the water-solubility, but also efficiently prevent the formation of metal ion-initiated precipitation.

Investigation on the *in vivo* subcutaneous phantom showed that the signals between MRI and PAI had good linear relationship (Figure S12). In addition, the slope of enhanced PA signal with different concentrations was higher than that of MRI signal, indicating the PAI imaging of MNP was more sensitive than the MRI imaging. Moreover, because of their easy conjugation with targeting groups, the MNPs modified with RGD exhibited the tumor targeting ability to the  $\alpha_\beta\beta_3$  integrin overexpressed on the surface of tumor vasculatures and the U87MG tumor cells (from PET data), which afforded RGD-conjugated MNPs higher accumulation capability in tumor than those RAD-modified MNPs through enhanced permeability and retention (EPR) effect. This further indicated that MNPs can conveniently function as a good nanoplatform for targeted imaging.

Though it is difficult to compare the imaging effects of our platform with other type of nanoplatforms (considering the lack of the triplemodality analogues), we demonstrated the unique ability of MNP nanoplatform to combine PET, photoacoustic and MR imaging modalities together to get complementary information for tumor imaging. For example, PET efficiently provides the *in vivo* pharmacokinetics and biodistribution of the nanoprobes and can also provide physiological information on disease with whole body imaging capability, but it cannot image tissues at high spatial resolution; PAI provides functional and molecular information on the tumor with high spatial resolution. It is a cheap and convenient way to image tumor in real time but suffers from limited tissue penetration ability, which can be compensated by PET. MRI provides high spatial resolution image and anatomical information on disease but generally lacks of molecular imaging capability. Combination of PET/PAI/MRI thus allows us to image diseases at different depths with molecular and anatomical information.

Recent developments showed that multimodality imaging is promising not only for accurate tumor imaging but also for guiding tumor resection. For example, PET/MRI, which combines the exquisite anatomical information by MRI with the extreme sensitivity of PET, can be used for whole-body imaging and deep tumor localization. MRI/fluorescence imaging (FI) is appropriate for guiding superficial tumor resection. In comparison, combining PET/MRI/PAI together is anticipated to help for guiding both superficial and deep tumor surgery. To our knowledge, no such triple-modality nanoplatform was reported so far. Accordingly, our triple-modality MNP system can be first used for PET and MRI to obtain the detailed information on tumor for surgical planning in presurgery. PAI can then be used to localize the superficial and relatively deep tumors in surgery for helping the tumor resection. Overall, a reliable method for preparation of water-soluble MNP has been developed in our work, which lays down a foundation for its future biomedical applications. It can be easily envisioned that MNP can serve as a nanoplatform not only for molecular imaging but also for theranostics. Considering the abundant functionalities of melanin, such as binding drugs,<sup>46</sup> MNP-based platform used for drug delivery and therapy are now being investigated.

## CONCLUSION

In conclusion, we report MNP as the natural biomarker-transferred active platform for multimodality imaging. MNP is of particular interest because such an endogenous agent with native photoacoustic signals and strong chelating properties with metal ions can act as an active platform to simplify the assembling of different imaging moieties. MNP can be easily modified with biomolecules for targeted tumor multimodality imaging, and it showed good *in vivo* tumor imaging properties. We expect this work will stimulate further studies of multifunctional endogenous material as nanoplatforms for potential imaging and therapeutic applications.

## MATERIALS AND METHODS

**Materials.** The following reagents were acquired and used as received: melanin (Sigma-Aldrich), sodium hydroxide (Sigma-Aldrich), hydrochloric acid (37 wt %, Sigma-Aldrich),  $\text{NH}_4\text{OH}$  solution (28 wt %, Sigma-Aldrich), amine-PEG<sub>5000</sub>-amine ( $\text{NH}_2\text{-PEG}_{5000}\text{-NH}_2$ , 5 kDa, Laysan Bio), dimethylthiazolyl-diphenyltetrazo-

lium (MTT; Biotium), phosphate buffered saline (PBS, Gibco), and agarose (Invitrogen). Millipore water (at 18 MΩ) was used.

**Preparation of PWS-MNP.** Tyrosine-derived synthetic melanin (20 mg) was first dissolved in 10 mL of 0.1 N NaOH aqueous solution under vigorous stirring. After dissolving, HCl aqueous solution (0.1 N) was swiftly dropped into the obtained basic melanin solution to adjust the pH to 7.0 under sonication with output power = 10 W for 1 min. A bright black melanin aqueous solution was obtained. The neutralized solution was further centrifuged with a centrifugal-filter (Amicon centrifugal filter device, MWCO = 30 kDa) and washed with deionized water and repeated several times to remove the produced NaCl. The aqueous solvent was removed by freeze-drying to obtain 15 mg black solid of PWS-MNP.

**Surface Modification of MNP with NH<sub>2</sub>-PEG<sub>5000</sub>-NH<sub>2</sub> (PEG-MNP).** NH<sub>4</sub>OH solution (28 wt %) was added to 5 mL of PWS-MNP aqueous solution (1 mg/mL of water) to adjust the pH of the solution to 9. This mixed solution was added dropwise into NH<sub>2</sub>-PEG<sub>5000</sub>-NH<sub>2</sub> (5, 10, 25, and 50 mg) aqueous solution with pH = 9. After vigorous stirring for 12 h, PEG-modified MNP was retrieved by centrifugation with a centrifugal-filter (Amicon centrifugal filter device, MWCO = 30 kDa) and washed with deionized water several times by redispersion/centrifugation processes to remove the unreacted NH<sub>2</sub>-PEG<sub>5000</sub>-NH<sub>2</sub>. The aqueous solvent was removed by freeze-drying and the obtained PEG-MNP was weighed to preliminary calculate the quantity of the PEG attached on MNPs. Because of the existence of one NH<sub>2</sub> group per PEG chain on the surface of MNP, we then accurately determined the NH<sub>2</sub> group on MNP with fluorescamine by spectrofluorometer to calculate the amount of PEG on the nanoparticles (using ethamine as the standard).

**Conjugation of PEG-MNP with RGD (RGD-PEG-MNPs).** The cross-linker solution was prepared freshly. The 4-(*N*-maleimidomethyl)cyclohexane-1-carboxylic acid 3-sulfo-*N*-hydroxysuccinimide ester sodium salt (sulfo-SMCC) (1.2 mg) was first dissolved in 36 μL of dimethyl sulfoxide (DMSO). The water-soluble PEG-MNP [1 mg in 1 mL of PBS (pH = 7.2)] was incubated with the above cross-linker solution for 2 h at room temperature. The resultant thiol-active MNP ran through a PD-10 column prewashed with PBS (pH = 7.2, 10 mM) to remove the excessive sulfo-SMCC and byproducts. The purified MNP was concentrated to the final volume of 0.5 mL with a centrifugal-filter (MWCO = 30 kDa). The cRGDFC stock solution (120 μL of 5 mM in the degassed water) was added to the above MNP solution with stirring. The conjugation reaction proceeded for 24 h at 4 °C. The uncoupled RGD peptide was removed through a PD-10 column and collected to analyze its quantity through HPLC. The number of coupled RGD on one MNP was then calculated. The resultant product, RGD-PEG-MNP, were concentrated by a centrifugal-filter (MWCO = 30 kDa) and stored at 4 °C for one month without losing targeting activity. The final RGD-PEG-MNP were reconstituted in PBS and filtered through a 0.22 μm filter for cell and animal experiments.

**Preparation of Fe<sup>3+</sup> or Cu<sup>2+</sup> chelated RGD-PEG-MNPs and PEG-MNPs.** The MNP (1 mg in 1 mL H<sub>2</sub>O) was labeled with Fe<sup>3+</sup> or Cu<sup>2+</sup> by addition of 20 μL of fresh FeCl<sub>3</sub> (10 mg/mL) in PBS (pH = 7.4) or 20 μL of CuCl<sub>2</sub> (10 mg/mL) in buffer solution of pH = 5.5 followed by a 1 h incubation at 40 °C (the chelating mechanisms of MNPs were shown in Figure S13). The labeled complexes were then purified by a PD-10 column. The products were washed out by PBS and passed through a 0.22-μm Millipore filter into a sterile vial for in vitro and animal experiments. The Fe<sup>3+</sup> and Cu<sup>2+</sup> concentrations of MNPs were measured by inductively coupled plasma-mass spectrometry (ICP-MS) analysis. The stability of metal ion-chelated MNPs were studied by incubating those MNPs in PBS (pH = 7.4) at 37 °C. Those MNPs were placed in dialysis tube (MWCO 10K) with magnetic stirring, dialysis against 10 mL PBS. At a certain time, dialysate was removed for ICP-MS analysis and replaced with fresh PBS solution. For ICP-MS analysis, 100 μL of the detected sample was first heated to evaporate the water solvent and then digested with 0.5 mL of concentrated nitric acid (70% w/w) under heating. After the solvent was evaporated, the residue was then dissolved in 7 mL of dilute nitric acid (2% w/w) for final ICP-MS analysis.

**Characterization of MNPs.** FT-IR spectra were measured in a transmission mode on a Bio-Rad FT-IR spectrophotometer (Model FTS135) under ambient conditions. Samples of pristine melanin granules and functionalized MNPs were ground with KBr and then compressed into pellets. Transmission electron microscopy (TEM) images were recorded on a JEOL 2010 transmission electron microscope at an accelerating voltage of 100 kV. The TEM specimens were made by placing a drop of the nanoparticle aqueous solution on a carbon-coated copper grid. The hydrodynamic sizes of the MNPs were determined by dynamic light scattering (DLS) using a 90 Plus particle size analyzer (Malvern, Zetasizer Nano ZS90). Zeta potentials were measured using a zeta potential analyzer (Malvern, Zetasizer Nano ZS90). The <sup>1</sup>H NMR spectra were recorded at 20 °C on a 400 MHz NMR spectrometer (Bruker), using D<sub>2</sub>O as solvent.

**<sup>64</sup>Cu<sup>2+</sup> Radiolabeling.** The MNPs with or without Fe<sup>3+</sup> were further radiolabeled with <sup>64</sup>Cu<sup>2+</sup> by addition of 1–1.5 mCi of <sup>64</sup>CuCl<sub>2</sub> in 0.1 N NaOAc (pH 5.5) buffer followed by 1 h incubation at 40 °C. The radiolabeled MNPs were then purified by a PD-10 column (GE Healthcare, Piscataway, NJ, USA). The product was washed out by PBS and passed through a 0.22-μm Millipore filter into a sterile vial for in vitro and animal experiments. The investigation of the radiolabeling stability of MNPs is similar to the metal ion-chelated MNPs except that the detector ICP-MS was replaced by PerkinElmer 1470 automatic gamma-counter for counting radioactivity.

**Cell Viability.** In vitro cytotoxicity of MNPs was determined in NIH-3T3 and U87MG cells by the MTT assay. NIH-3T3 and U87MG cells were incubated on 96-well plate in DMEM medium containing 10% FBS and 1% penicillin/streptomycin at 37 °C in 5% CO<sub>2</sub> humidified atmosphere for 24 h and 0.5 × 10<sup>4</sup> cells were seeded per well. Cells were then cultured in the medium supplemented with indicated doses of different MNPs for 24 h. The final concentrations of MNPs in the culture medium were fixed at 3.125, 6.25, 12.5, and 25 μM in the experiment. Addition of 10 μL of MTT (0.5 mg/mL) solution to each well and incubation for 3 h at 37 °C was followed to produce formazan crystals. Then, the supernatant was removed and the products were lysed with 200 μL of DMSO. The absorbance value was recorded at 590 nm using a microplate reader. The absorbance of the untreated cells was used as a control and its absorbance was as the reference value for calculating 100% cellular viability.

**In Vitro Cell Uptake.** U87MG cells (1 × 10<sup>5</sup> per well) were seeded in 12-well tissue culture plates and allowed to attach overnight. The cells were washed twice with serum-free DMEM and incubated with the <sup>64</sup>Cu-labeled MNPs (2 μCi per well, final concentration approximately 6 nM) in 400 μL of serum-free DMEM at 37 °C. The specific binding of the probes with U87MG cells was determined by coincubation with RGD (30 μg per well). After 1, 2, and 4 h, the cells were washed three times with cold PBS and lysed with the addition of 200 μL of 0.2 M NaOH. The radioactivity of all fractions was counted using a PerkinElmer 1470 automatic gamma-counter. The uptake (counts per minute) was expressed as the percentage of added radioactivity.

**PAI Analysis of Phantom.** For studying the PAI properties of MNPs, a cuboid container was half filled with 1% agarose gel to half depth. Different concentrations of MNPs aqueous solutions ranging from 0.625 to 20 μM were filled into polyethylene capillaries and then the capillaries were laid on the surface of solidified agarose gel. The capillaries were further covered with thin 1% agarose gel to make the surface smooth. For the particle's sensitivity in living body, MNPs aqueous solutions with different concentrations from 5 μM to 80 μM were mixed with matrigel at 0 °C and then subcutaneously injected on the lower back of mice. The PAIs of the mixtures were collected after they were solidified.

The Vevo LAZR PAI System (VisualSonics Inc., Toronto, Canada) with a laser at excitation wavelength of 680 nm and a focal depth of 10 mm was used to acquire photoacoustic and ultrasound images. Image analysis was carried out using ImageJ. Briefly, quantification analysis was performed on the PAI images. ROIs were drawn over the sample on the PAI images. The PAI signal intensity was then measured using the ROIs manager tool.

**MRI Analysis of Phantom.** MRI experiments were performed at 25 °C in a magnetic resonance (MR) scanner (Siemens 1.0 T). To simulate the biological environment, agarose gel, prepared in 300 μL of the PCR tube using secondary distilled water as the solvent for dissolving the agarose, was used to demonstrate the magnetic signal. The bottom of the tube was first covered with a layer of 1% agarose gel. When agarose gel was cooled, the mixtures of MNPs and aqueous solution of agarose (ratio 1:1 by volume) with iron concentrations at 62.5, 125, 250, 500, and 1000 μM Fe (amount to 1.25, 2.5, 5, 10, 20 μM MNP), were then filled into the intermediate portion of the PCR tube respectively while the sample was hot. After cooling, another 1% agarose gel was covered on the top layer of the cube. The tubes were placed into the MR scanner and a number of MR sequences were run, spin-echo for R<sub>1</sub> determination (TR: 50–3000 ms; TE: 5.5 ms, flip angle 30°; FOV: 3.5 cm, matrix: 256 × 256; slice thickness: 1 mm). The luminance values of the resulting image were obtained through the ImageJ software processing, thereby calculating the R<sub>1</sub> value.

For measurement the MNPs' detection sensitivity in living subject, Fe-chelated MNPs aqueous solution with different concentrations from 1.25 μM to 20 μM were mixed with matrigel at 0 °C and then subcutaneous injected on the lower back of mice. The MRIs of the mixtures were collected after they were solidified. The used T<sub>1</sub>-flash MRI sequence is as follows: TR: 700 ms, TE: 5.2 ms; FOV: 3.5 cm, matrix: 256 × 256; slice thickness: 1 mm.

**Subcutaneous Tumor Models.** All animal experiments were performed in compliance with the Guidelines for the Care and Use of Research Animals established by the Stanford University Animal Studies Committee. Female athymic nude mice (nu/nu) in 4–6 weeks old were obtained from the Charles River Laboratories (Boston, MA, USA) and kept under sterile conditions. U87MG cells suspended in 100 μL of PBS were inoculated subcutaneously in the shoulder of nude mice. When the tumors reached 0.5–0.8 cm in diameter, the tumor bearing mice were subjected to *in vivo* multimodality imaging (PAI, MRI and PET) and biodistribution studies.

**PAI and MRI of Tumor Bearing Mice.** Mice bearing tumor (U87MG) were anesthetized with 2% isoflurane in oxygen and placed with lateral position. MRI was performed using the same instrument, protocols and conditions as in the phantom MRI study. Imaging analysis was performed using the ImagingJ software. The contrast was adjusted. PAI was carried out using the same Vevo LAZR PAI System as the *in vitro* study. Similarly, image analysis was carried out using ImageJ. Quantification analysis of PA and MR signals was performed on the PAI and MRI images. Because the enhanced signals of MRI and PAI in tumors were dispersed heterogeneously, the enhanced signal regions in tumors on the PAI and MRI images were used as ROIs to analysis the signal change with injection time (comparing the signal intensity at 4 h injection with 0 h injection).

**Small-Animal PET.** Small animal PET imaging of tumor-bearing mice was performed on a Siemens Inveon microPET-CT. Mice bearing U87-MG tumors were injected with <sup>64</sup>Cu-labeled MNPs ( $110.0 \pm 5.0 \mu\text{Ci}$ ) via the tail vein. At different times after injection (2, 4, and 24 h), the mice were anesthetized with 2% isoflurane and placed prone near the center of the FOV of the scanner. Three-minute static scans were obtained. All the small animal PET images were reconstructed using Irw4.0 software by two-dimensional ordered-subsets expectation maximization (OSEM) algorithm. No background correction was performed. The radioactivity uptake in the tumor and normal tissues was calculated using a region of interest (ROI) drawn over the whole organ region and expressed as a percentage of the injected radioactive dose per gram of tissue (% ID/g).

## ASSOCIATED CONTENT

### Supporting Information

Additional figures and table. This material is available free of charge via the Internet at <http://pubs.acs.org>.

## AUTHOR INFORMATION

### Corresponding Author

zcheng@stanford.edu

## Author Contributions

<sup>#</sup>Quli Fan and Kai Cheng contributed equally to this work.

## Notes

The authors declare no competing financial interest.

## ACKNOWLEDGMENTS

This work was supported, in part, by the Office of Science (BER), U.S. Department of Energy (DE-SC0008397), NCI of Cancer Nanotechnology Excellence Grant CCNE-TR US4 CA119367, CA151459, NIH In Vivo Cellular Molecular Imaging Center (ICMIC) Grant P50 CA114747, the National Basic Research Program of China (No. 2012CB723402), the National Natural Science Foundation of China (No. 21222404, 61378081) and NY211003.

## REFERENCES

- (1) Tan, S. J.; Campolongo, M. J.; Luo, D.; Cheng, W. L. *Nat. Nanotechnol.* **2011**, *6*, 268–276.
- (2) Rinker, S.; Ke, Y.; Liu, Y.; Chhabra, R.; Yan, H. *Nat. Nanotechnol.* **2008**, *3*, 418–422.
- (3) Ke, Y.; Ong, L. L.; Shih, W. M.; Yin, P. *Science* **2012**, *338*, 1177–1183.
- (4) Schnepf, Z. *Angew. Chem., Int. Ed.* **2012**, *52*, 1096–1108.
- (5) Godin, B.; Tasciotti, E.; Liu, X.; Serda, R. E.; Ferrari, M. *Acc. Chem. Res.* **2011**, *44*, 10979–10989.
- (6) Parodi, A.; Quattrochi, N.; van de Ven, A. L.; Chiappini, C.; Evangelopoulos, M.; Martinez, J. O.; Brown, B. S.; Khaled, S. Z.; Yazdi, I. K.; Enzo, M. V.; Isenhart, L.; Ferrari, M.; Tasciotti, E. *Nat. Nanotechnol.* **2012**, *8*, 61–68.
- (7) Weissleder, R.; Pittet, M. J. *Nature* **2008**, *452*, 580–589.
- (8) Tassa, C.; Shaw, S. Y.; Weissleder, R. *Acc. Chem. Res.* **2008**, *41*, 842–852.
- (9) Michalet, X.; Pinaud, F. F.; Bentolila, L. A.; Tsay, J. M.; Doose, S.; Li, J. J.; Sundaresan, G.; Wu, A. M.; Gambhir, S. S.; Weiss, S. *Science* **2005**, *307*, 538–544.
- (10) Zhou, M.; Zhang, R.; Huang, M.; Lu, W.; Song, S. L.; Melancon, M. P.; Tian, M.; Liang, D.; Li, C. *J. Am. Chem. Soc.* **2010**, *132*, 15351–15358.
- (11) Wang, Y. C.; Liu, Y. J.; Luehmann, H.; Xia, X. H.; Wan, D. H.; Cutler, C.; Y. N. Xia, Y. N. *Nano Lett.* **2013**, *13*, 581–585.
- (12) Luo, S. L.; Zhang, E. L.; Su, Y. P.; Cheng, T. M.; Shi, C. M. *Biomaterials* **2011**, *32*, 7127–7138.
- (13) Seo, J.; Ren, G.; Liu, H. G.; Miao, Z.; Park, M.; Wang, Y. H.; Miller, T. M.; Barron, A. E.; Cheng, Z. *Bioconjugate Chem.* **2012**, *23*, 1069–1079.
- (14) Werner, E. J.; Datta, A.; Jocher, C. J.; Raymond, K. N. *Angew. Chem., Int. Ed.* **2008**, *47*, 8568–8580.
- (15) Jimbow, K.; Miyake, Y.; Homma, K.; Yasuda, K.; Izumi, Y.; Tsutsumi, A.; Ito, S. *Cancer Res.* **1984**, *44*, 1128–1134.
- (16) Prota, G. *Pigm. Cell Res.* **2000**, *13*, 283–293.
- (17) Iozumi, K.; Hoganson, G. E.; Pennella, R.; Everett, M. A.; Fuller, B. B. *J. Invest. Dermatol.* **1993**, *100*, 806–811.
- (18) Seagle, B.-L. L.; Rezai, K. A.; Kobori, Y.; Gasyna, E. M.; Rezaei, K. A.; Norris, J. R. *Proc. Natl. Acad. Sci. U. S. A.* **2005**, *102*, 8978–8983.
- (19) Lu, S.; Fan, Q.-L.; Chua, S.-J.; Huang, W. *Macromolecules* **2003**, *36*, 304–310.
- (20) Moghimi, S. M.; Hunter, A. C.; Murray, J. C. *Pharmacol. Rev.* **2001**, *53*, 283–318.
- (21) Lee, H.; Dellatore, S. M.; Miller, W. M.; Messersmith, P. B. *Science* **2007**, *318*, 426–430.
- (22) Zerda, A. D. L.; Zavaleta, C.; Keren, S.; Vaithilingam, S.; Bodapati, S.; Liu, Z.; Levi, J.; Smith, B. R.; Ma, T.-J.; Oralkan, O.; Cheng, Z.; Chen, X. Y.; Dai, H. J.; Khuri-Yakub, B. T.; Gambhir, S. S. *Nat. Nanotechnol.* **2008**, *3*, 557–562.
- (23) Zerda, A. D.; Bodapati, S.; Teed, R.; May, S. Y.; Tabakman, S. M.; Liu, Z.; Khuri-Yakub, B. T.; Chen, X. Y.; Dai, H. J.; Gambhir, S. S. *ACS Nano* **2012**, *6*, 4694–4701.

- (24) Cheng, Z.; De Jesus, O. P.; Kramer, D. J.; De, A.; Webster, J. M.; Gheysens, O.; Levi, J.; Namavari, M.; Wang, S.; Park, J. M.; Zhang, R.; Liu, H. G.; Lee, B.; Syud, F. A.; Gambhir, S. S. *Mol. Imaging Biol.* **2010**, *12*, 316–324.
- (25) Nielsen, C. H.; Kimura, R. H.; Withofs, N.; Tran, P. T.; Miao, Z.; Cochran, J. R.; Cheng, Z.; Felsher, D.; Kjær, A.; Willmann, J. K.; Gambhir, S. S. *Cancer Res.* **2010**, *70*, 9022–9030.
- (26) Hoppmann, S.; Miao, Z.; Liu, S. L.; Liu, H. G.; Ren, G.; Bao, A.; Cheng, Z. *Bioconjugate Chem.* **2011**, *22*, 413–421.
- (27) Lovell, J. F.; Jin, C. S.; Huynh, E.; Jin, H. L.; Kim, C.; Rubinstein, J. L.; Chan, W. C. W.; Cao, W. G.; Wang, L. V.; Zheng, G. *Nat. Mater.* **2011**, *10*, 324–332.
- (28) Huynh, E.; Lovell, J. F.; Helfield, B. L.; Jeon, M.; Kim, C.; Goertz, D. E.; Wilson, B. C.; Zheng, G. *J. Am. Chem. Soc.* **2012**, *134*, 16464–16467.
- (29) Liu, T. W.; MacDonald, T. D.; Jin, C. S.; Gold, J. M.; Bristow, R. G.; Wilson, B. C.; Zheng, G. *ACS Nano* **2013**, *7*, 4221–4232.
- (30) Simon, J. D.; Hong, L.; Peles, D. N. *J. Phys. Chem. B* **2008**, *112*, 13201–13217.
- (31) Cheng, Z.; Mahmood, A.; Li, H.; Davison, A.; Jones, A. G. *Cancer Res.* **2005**, *65*, 4979–4986.
- (32) Cheng, Z.; Zhang, L.; Graves, E.; Xiong, Z. M.; Dandekar, M.; Chen, X. Y.; Gambhir, S. S. *J. Nucl. Med.* **2007**, *48*, 987–994.
- (33) Ren, G.; Miao, Z.; Liu, H. G.; Jiang, L.; Limpa-Amara, N.; Mahmood, A.; Gambhir, S. S.; Cheng, Z. *J. Nucl. Med.* **2009**, *50*, 1692–1699.
- (34) Oh, J. T.; Stoica, G.; Wang, L. V.; Li, M.-L.; Zhang, H. F.; Maslov, K. *J. Biomed. Opt.* **2006**, *11*, 34032.
- (35) Wang, Y.; Maslov, K.; Zhang, Y.; Hu, S.; Yang, L.; Xia, Y. N.; Liu, J.; Wang, L. V. *J. Biomed. Opt.* **2011**, *16*, 011014.
- (36) Hong, L.; Simon, J. D. *J. Phys. Chem. B* **2007**, *111*, 7938–7947.
- (37) Samokhvalov, A.; Liu, Y.; Simon, J. D. *Photochem. Photobiol.* **2004**, *80*, 84–88.
- (38) Liu, Y.; Hong, L.; Kempf, V. R.; Wakamatsu, K.; Ito, S.; Simon, J. D. *Pigm. Cell Res.* **2004**, *17*, 262–269.
- (39) Woodruff, W. W. J.; Djang, W. T.; McLendon, R. E.; Heinz, E. R.; Voorhees, D. R. *Radiology* **1987**, *165*, 209–213.
- (40) Ginat, D. T.; Meyers, S. P. *Radiographics* **2012**, *32*, 499–516.
- (41) Paproski, R. J.; Forbrich, A.; Harrison, T.; Hitt, M.; Zemp, R. J. *J. Biomed. Opt.* **2011**, *16*, 080503.
- (42) Qin, C. X.; Cheng, K.; Chen, K.; Hu, X.; Liu, Y.; Lan, X. L.; Zhang, Y. X.; Liu, H. G.; Xu, Y. D.; Bu, L. H.; Su, X. H.; Zhu, X. H.; Meng, S. X.; Cheng, Z. *Sci. Rep.* **2013**, *3*, 1490.
- (43) Stritzker, J.; Kirscher, L.; Scadeng, M.; Deliolanis, N. C.; Morscher, S.; Symvoulidis, P.; Schaefer, K.; Zhang, Q.; Buckel, L.; Hess, M.; Donat, U.; Bradley, W. G.; Ntzachristos, V.; Szalay, A. A. *Proc. Natl. Acad. Sci. U. S. A.* **2013**, *110*, 3316–3320.
- (44) Hong, S.; Na, Y. S.; Choi, S.; Song, I. T.; Kim, W. Y.; Lee, H. *Adv. Funct. Mater.* **2012**, *22*, 4711–4717.
- (45) Ceylan, H.; Urel, M.; Erkal, T. S.; Tekinay, A. B.; Dana, A.; Guler, M. O. *Adv. Funct. Mater.* **2013**, *23*, 2081–2090.
- (46) Ings, R. M. *J. Drug Metab. Rev.* **1984**, *15*, 1183–1212.